Data-driven systematic parameter identification of an electrochemical model for lithium-ion batteries with artificial intelligence

Weihan Li[a,b,1,*], Iskender Demir[a,1], Decheng Cao[a], Dominik Jöst[a,b], Florian Ringbeck[a,b], Mark Junker[a,b], Dirk Uwe Sauer[a,b,c]

[a] *Chair for Electrochemical Energy Conversion and Storage Systems, Institute for Power Electronics and Electrical Drives (ISEA), RWTH Aachen University, Jaegerstrasse 17/19, 52066, Aachen, Germany*
[b] *Juelich Aachen Research Alliance, JARA-Energy, Germany*
[c] *Helmholtz Institute Münster (HI MS), IEK-12, Forschungszentrum Jülich, Germany*

Abstract

Electrochemical models are more and more widely applied in battery diagnostics, prognostics and fast charging control, considering their high fidelity, high extrapolability and physical interpretability. However, parameter identification of electrochemical models is challenging due to the complicated model structure and a large number of physical parameters with different identifiability. The scope of this work is the development of a data-driven parameter identification framework for electrochemical models for lithium-ion batteries in real-world operations with artificial intelligence, i.e., the cuckoo search algorithm. Only current and voltage data are used as input for the multi-objective global optimization of the parameters considering both voltage error between the model and the battery and the relative capacity error between two electrodes. The multi-step identification process based on sensitivity analysis increases the identification accuracy of the parameters with low sensitivity. Moreover, the novel identification process inspired by the training process in machine learning further overcomes the overfitting problem using limited battery data. The data-driven approach achieves a maximum root mean square error of 9 mV and 12.7 mV for the full cell voltage under constant current discharging and real-world driving cycles, respectively, which is only 17.9% and 42.9% of that of the experimental identification approach.

Keywords: lithium-ion, battery, electrochemical model, parameter identification, artificial intelligence

1. Introduction

1.1. Motivation

Driven by both political and technological initiatives towards ecological mobility, transportation electrification in various areas, such as vehicles, trains, ships and aircraft, is becoming more and more popular.

*Corresponding author. Chair for Electrochemical Energy Conversion and Storage Systems, Institute for Power Electronics and Electrical Drives (ISEA), RWTH Aachen University, Jaegerstrasse 17/19, 52066, Aachen, Germany
Email address: weihan.li@isea.rwth-aachen.de (Weihan Li)
[1] Equal contribution

Among all the energy sources for the electrified transportation applications, such as plug-in hybrid electric vehicles (PHEVs), hybrid electric vehicles (HEVs), and electric vehicles (EVs), the lithium-ion battery (LIB) is one of the most promising candidates, combining high energy density, low self-discharge, long lifetime and reliable safety [1]. Over the past years, significant research has been conducted to build sophisticated models in different scales to estimate and predict battery dynamics. Compared with equivalent circuit models (ECMs), which are used in most battery management systems (BMSs), the electrochemical models (EMs) promise numerous improvements considering extrapolation ability and physical representation of battery internal states, especially under extreme conditions.

Although various research has been conducted to accomplish tasks in BMS based on EMs, such as state estimation [2–4], aging identification [5], power prediction [6] and fast charging control [7], fast and accurate identification of all the parameters in the EMs for new batteries remains as one of the challenges due to a large number of parameters with various sensitivities and the high nonlinearity and complexity of the battery model. While the formulation of the model equations in EMs can also be dealt with abstractly for all batteries with different chemistry, the parameterization must be carried out individually for each specific cell as the parameter values may vary due to different cell designs. Conclusions about the internal states of the battery can only be drawn if an accurate parameter set of the model is provided. Ecker et al. [8, 9] determined and parameterized an EM for an NMC/graphite pouch cell experimentally by opening the cell under an argon atmosphere and measuring the parameters with various laboratory apparatus. Similarly, Schmalstieg et al. [10, 11] further extracted the physical parameters together with thermal parameters from a high-power prismatic cell by opening the cell and measuring the parameters experimentally. Although these pioneering work provided not only parameter values for specific cells but also the determination procedures in detail, invasive parameter identification steps can be very time-consuming, expensive and lack accuracy for some dynamic applications.

1.2. Literature review

Although the poor identifiability of the model parameters caused by nonlinearities, redundant definitions, intertwined physical phenomena and time-scale separations in battery dynamics [12] is a great challenge, data-driven non-invasive methods are attracting more and more attention from both industry and academy due to the cost and time reduction compared with invasive experimental procedures. In some cases, the cells are even not allowed to be opened for the post-mortem measurement due to a non-disclosure agreement with the cell manufacturer, which further raises the requirements on accurate and fast data-driven parameter identification methods. Among the approaches found in the literature, various gradient-based nonlinear least-square regression algorithms have been used widely to identify the parameters by minimizing the sum of the squared voltage errors. Boovaragavan et al. [13] estimated four transport and kinetic parameters using a reformulated EM for an LCO/graphite cell. Similarly, Ramadesigan et al. [14] identified effective

kinetic and transport parameters from experimental data. In both cases, the Jacobian-based Gauss-Newton method was used to solve the nonlinear regression problem. Considering the better efficiency over the Gauss' algorithm in dealing with nonlinear problems, Santhanagopalan et al. [15] identified five parameters under constant charge and discharge currents for the pseudo-2-dimension (P2D) model and a reformulated EM, respectively, using the Levenberg-Marquardt method. In Ref. [16], nine parameters were identified with the same algorithm for a reduced-order EM. However, no experimental validation with a LIB cell was carried out to verify the identification reliability. Schmidt et al. [17] further increased the number of identifiable parameters by adding the number of experiment datasets, which exposed the contribution of the increase of experimental data to a successful parameter identification. A total of 24 parameters were identified with the pattern search algorithm for an extended single particle model.

With the success of artificial intelligence, especially the metaheuristic algorithms, which is a group of bio-inspired gradient-free iterative optimization processes that are immune to local minimum traps [18] in solving the global optimization problems in other research fields, more and more research was conducted successfully in identifying the physical parameters of EMs. Genetic algorithm (GA) is one of the most frequently used metaheuristic algorithms for data-driven parameter identification [19–28]. Forman et al. [19] assessed the parameter identifiability with Fisher information and identified a set of 88 parameters of a P2D model by GA based on constant-current charge and discharge dataset. However, the dataset doesn't include the data with high dynamics, which are essential for the identification of impedance-related parameters. The identification of a large number of insensitive parameters not only increases the computation burden exponentially but also doesn't contribute to any significant model performance increase. Zhang et al. [21, 22] proposed a multi-objective optimization approach considering both voltage and temperature error of the model for the identification of 25 parameters with GA. In comparison, Li et al. [23] proposed a divide-and-conquer strategy to divide the full set of P2D parameters into two groups for separate identification with GA. However, the identified parameters were not validated under other experimental conditions. In Ref. [24], Pang et al. proposed a systematic parameter identification scheme to conduct the identification of 16 parameters for an extended SPM with GA and validation against the different experimental data acquired from a 2 Ah NMC/graphite cell.

Compared with GA, particle swarm optimization (PSO) has an inbuilt guidance strategy, which offers distinct notable advantages, e.g., greater diversity and exploration, faster convergence and more variety in search trajectories. The use of memory to store the previous best solutions obtained by every candidate results in faster convergence and higher robustness of PSO. Therefore, it has also been used in the identification of parameters for both ECMs [29] and EMs [30]. Rahman et al. [30] tracked the change of four parameters of a cylindrical cell with an LCO cathode during aging by PSO. Yang et al. [31] identified 16 physical parameters based on the discharge experiment of 0.5 C with PSO. Chu et al. [32] designed a multi-step approach to identify different parameters divided by frequency decomposition in each step and

the reformulated EM with the identified parameters was validated experimentally under a standard driving cycle. Moreover, Fan et al. [33] further proposed a two-step parameter identification approach based on a large number of experimental datasets to identify 26 parameters for an NMC/graphite battery cell. Although GA and PSO are widely used in parameter identification of the EMs, the identification efficiency and accuracy need to be further increased in both algorithm and methodology level considering the industry need. Furthermore, parameter overfitting is a regular problem due to the lack of data as a result of the required short testing time, which needs to be solved by redesigning the whole data-driven identification framework. There is also rare work comparing the identification accuracy between the experimental method and the data-driven method.

1.3. Contributions

This paper aims to bridge the aforementioned research gap and proposes a data-driven approach using artificial intelligence, i.e., the cuckoo search algorithm, to identify the parameters of EMs in real-world operation. The comprehensive benchmarking of the parameter values in literature defines the boundary values of the parameters in electrodes and electrolytes with the same chemistry, remaining the physical meaning of the parameters. Parameter sensitivity analysis was further carried out to categorize the total 26 parameters into three groups with high, medium and low sensitivity. The proposed framework only uses the current and voltage data of a battery to identify the parameters. Not only voltage error between model and cell but also capacity error between two electrodes are defined as optimization objectives, which reduces the identification errors of the capacity-related parameters. Furthermore, the multi-step identification approach considering the differences of the parameter sensitivities increases the identification accuracy of the parameters with lower sensitivity. The proposed framework was first validated numerically with a virtual cell and compared with other data-driven methods considering the identification errors of parameters, computation efficiency and convergence speed. The verification of the data-driven parameter identification framework with an NMC/graphite commercial cell experimentally further highlights the robustness and reliability of the approach compared with invasive experimental identification methods.

2. Electrochemical modeling

The P2D model developed by Doyle et al. [34] describes the solid and electrolyte dynamics of LIBs in the positive electrode, separator and negative electrode. On the macroscopic scale, the chemical reaction kinetics are assumed to influence the battery dynamics only in x-dimension, where lithium ions can transfer in the electrolyte throughout all domains in the liquid phase. On the microscopic scale, the solid particles in both electrodes are assumed to be spheres with specific radii, and lithium ions can diffuse along the r-dimension inside the solid phase. As shown in the schematic of the P2D model in Fig. 1, the whole

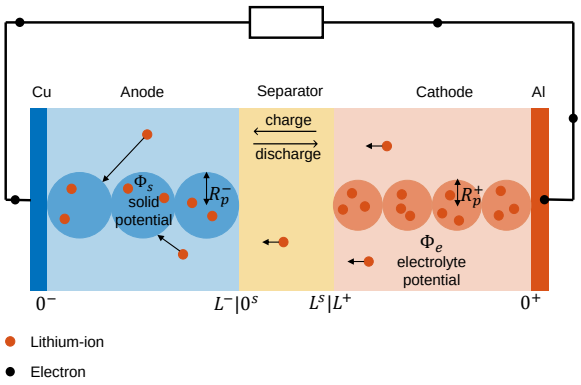

Figure 1: Schematic of the electrochemical modeling for LIBs

LIB is divided into three different domains, i.e., anode (ranges from 0^- to L^-), separator (ranges from 0^s to L^s) and cathode (ranges from L^+ to 0^+). The particles represent the porous electrodes and are surrounded by the electrolyte, and the electrodes are separated by the separator. During charging, lithium ions deintercalate from the active material in the positive electrode and move into the electrolyte solution. By diffusion and ionic conduction, the lithium ions transport through the separator and arrive at the surface of the negative electrode and finally intercalate into the active material. Several coupled nonlinear partial algebraic differential equations (PDAEs) map the transport processes of lithium ions in spatial and temporal terms within the electrode and the electrolyte, which are summarized together with the boundary conditions in Table 1. Both the concentration of lithium ions in electrodes and electrolyte, i.e., $c_s(r, x, t)$ and $c_e(x, t)$, and the potentials within the cell, i.e., solid potential, $\Phi_s(x, t)$, electrolyte potential, $\Phi_e(x, t)$, open-circuit potential (OCP), $U(x, t)$, and lithium-intercalation overpotential, $\eta(x, t)$, can be derived from these equations. To consider the properties of the battery materials, effective conductivity and diffusion coefficients with "eff" suffixes are used based on Bruggeman's theory. Moreover, $a = (3/R_p)\varepsilon_s$ represents the specific interfacial area, $\alpha_a = \alpha_c = 0.5$ are the charge transfer coefficients, and the descriptions of the other parameters are summarized in Table 2. The readers are referred to [35] for further derivation details.

Most numerical methods for model-based state estimation and parameter identification require the model to consist of ordinary differential equations (ODEs) or algebraic equations (AEs) rather than PDAEs. The model-order reduction process is very challenging to carry out in a way that is numerically stable and computationally efficient for a wide range of battery operating conditions and parameter sets. In this work, the PDAEs of the P2D model are transformed into ODEs and AEs using the finite-difference method [36] in micro-scale and the finite-volume method [37] in macro-scale. The number of discretization nodes for both micro-scale and macro-scale in each domain equals 10, considering the compromise between model accuracy and computational efficiency.

Mechanisms	Governing equations	Boundary conditions
Electrode mass transport	$\frac{\partial c_s(r,x,t)}{\partial t} = \frac{1}{r^2}\frac{\partial}{\partial r}\left(D_s r^2 \frac{\partial c_s(r,x,t)}{\partial r}\right)$	$\left.\frac{\partial c_s^i(r,x,t)}{\partial r}\right\|_{r=0} = 0,$ $\left.\frac{\partial c_s^i(r,x,t)}{\partial r}\right\|_{r=R_p^i} = -\frac{j(x,t)}{D_s^i}$
Electrolyte mass transport	$\frac{\partial c_e(x,t)}{\partial t} = \frac{\partial}{\partial x}\left(D_{e,\text{eff}}\frac{\partial c_e(x,t)}{\partial x}\right) + \frac{a(1-t_+^0)}{\varepsilon_e} j(x,t)$	$c_e(L^+,t) = c_e(L^s,t),$ $c_e(0^s,t) = c_e(L^-,t),$ $D_{e,\text{eff}}\left.\frac{\partial c_e(x,t)}{\partial x}\right\|_{x=L^+} = D_{e,\text{eff}}\left.\frac{\partial c_e(x,t)}{\partial x}\right\|_{x=L^s},$ $D_{e,\text{eff}}\left.\frac{\partial c_e(x,t)}{\partial x}\right\|_{x=0^s} = D_{e,\text{eff}}\left.\frac{\partial c_e(x,t)}{\partial x}\right\|_{x=L^-}$
Solid potential of particles	$\frac{\partial}{\partial x}\left(\sigma_{s,\text{eff}}\frac{\partial \phi_s(x,t)}{\partial x}\right) = aFj(x,t)$	$\sigma_{s,\text{eff}}\left.\frac{\partial \phi_s(x,t)}{\partial x}\right\|_{x=L^+,L^-} = \frac{-I(t)}{A},$ $\sigma_{s,\text{eff}}\left.\frac{\partial \phi_s(x,t)}{\partial x}\right\|_{x=0^-,0^+} = 0$
Electrolyte potential	$\frac{\partial}{\partial x}\left(\sigma_{e,\text{eff}}\frac{\partial \phi_e(x,t)}{\partial x} - \sigma_{e,\text{eff}}\frac{2RT(1-t_+^0)}{F}\cdot\frac{\partial ln c_e(x,t)}{\partial x}\right) = -aFj(x,t)$	$\left.\frac{\partial \phi_e(x,t)}{\partial x}\right\|_{x=0^+} = 0,$ $\left.\frac{\partial \phi_e(x,t)}{\partial x}\right\|_{x=L^-} = 0,$ $\sigma_{e,\text{eff}}\left.\frac{\partial \phi_e(x,t)}{\partial x}\right\|_{x=L^+} = \sigma_{e,\text{eff}}\left.\frac{\partial \phi_e(x,t)}{\partial x}\right\|_{x=L^s},$ $\sigma_{e,\text{eff}}\left.\frac{\partial \phi_e(x,t)}{\partial x}\right\|_{x=0^s} = \sigma_{e,\text{eff}}\left.\frac{\partial \phi_e(x,t)}{\partial x}\right\|_{x=L^-}$
Butler-Volmer equation	$j(x,t) = \frac{i_0(x,t)}{F}\left(\exp\left(\frac{\alpha_a F}{RT}\eta(x,t)\right) - \exp\left(-\frac{\alpha_c F}{RT}\eta(x,t)\right)\right)$ $\eta(x,t) = \phi_s(x,t) - \phi_e(x,t) - U\left(\frac{c_{ss}(x,t)}{c_{s,max}}\right) - FR_f j(x,t)$ $i_0(x,t) = \kappa_{\text{eff}} F c_e(x,t)^{\alpha_a}(c_{s,max} - c_{ss}(x,t))^{\alpha_a} c_{ss}(x,t)^{\alpha_c}$	
Terminal voltage	$V(t) = \phi_s(0^+,t) - \phi_s(0^-,t)$	

Table 1: Summary of the governing equations of a P2D-model.

3. Parameter sensitivity analysis

In contrast to ECMs, EMs consist of a large number of physical parameters, and the experimental identification process of these parameters is very complicated, expensive and time-consuming [8, 9]. To identify the parameters of the EM based on current and voltage data, reasonable parameter value ranges need to be provided to maintain the physical meaning of the identified parameters and the sensitivity of the parameters under the specific ranges needs to be analyzed before identification. As summarized in Table 2, the total 26 physical parameters are grouped into four categories, i.e., geometric parameters, transport parameters, kinetic parameters, and concentration parameters. The value ranges of these parameters are determined for NMC/graphite cells based on a comprehensive benchmarking with more than 25 pieces of literature and experimental measurement. The superscripts $+$, $-$ and s of the parameters represent cathode, anode and separator, respectively. To obtain the boundary values for the physical parameters, no other constraints except the cell materials are applied in the literature review of the parameter values in Table 2,

Category	Parameter	Unit	Description	Boundary	Reference	Sensitivity
Geometric parameters	L^+	μm	Cathode thickness	35 - 79	[8, 38–44]	High
	L^s	μm	Separator thickness	10 - 30	[8, 38–43, 45, 46]	Medium
	L^-	μm	Anode thickness	35 - 79	[8, 38–44]	High
	A	m^2	Electrode surface area	0.378 - 0.395	Measurement	High
	ε_s^+	-	Cathode active material volume fraction	0.35 - 0.5	[8, 38, 42, 44]	High
	ε_s^-	-	Anode active material volume fraction	0.4 - 0.5	[8, 38, 42, 44]	High
	ε_e^+	-	Cathode electrolyte volume fraction	0.27 - 0.45	[8, 38–41, 43, 44, 47]	Medium
	ε_e^s	-	Separator electrolyte volume fraction	0.4 - 0.55	[8, 38–44, 47]	Low
	ε_e^-	-	Anode electrolyte volume fraction	0.26 - 0.5	[8, 38–41, 43, 44, 47]	Medium
	R_p^+	μm	Cathode particle radius	1 - 11	[8, 40–42, 44, 45, 47]	High
	R_p^-	μm	Anode particle radius	1 - 11	[8, 40–42, 45, 47]	High
Transport parameters	D_s^+	$10^{-14} m^2 s^{-1}$	Cathode solid diffusion coefficient	1 - 10	[38, 40, 41, 43, 45, 47, 48]	High
	D_s^-	$10^{-14} m^2 s^{-1}$	Anode solid diffusion coefficient	1 - 10	[38, 40, 43, 45, 47, 48]	High
	D_e	$10^{-10} m^2 s^{-1}$	Electrolyte diffusion coefficient	1.5 - 4.5	[8, 39, 43, 49, 50]	Medium
	b^+	-	Cathode Bruggeman coefficient	1.3 - 1.7	[39, 45]	Low
	b^s	-	Separator Bruggeman coefficient	1.3 - 1.7	[39, 43, 45, 48]	Low
	b^-	-	Anode Bruggeman coefficient	1.3 - 1.7	[39, 45]	Low
	t_0^+	-	Transference number of lithium cation	0.25 - 0.43	[8, 38, 39, 43, 47–49, 51, 52]	Medium
	σ_s^+	Sm^{-1}	Cathode electrode conductivity	36 - 185	[53]	Low
	σ_s^-	Sm^{-1}	Anode electrode conductivity	$1 - 1 \cdot 10^4$	[54]	Low
Kinetic parameters	κ^+	$10^{-11} m^{2.5}/(mol^{0.5} s)$	Cathode reaction rate coefficient	1 - 10	[8, 38, 41, 42, 44]	High
	κ^-	$10^{-11} m^{2.5}/(mol^{0.5} s)$	Anode reaction rate coefficient	1 - 20	[8, 38, 41, 42]	High
	R_f	$10^{-3} \Omega m^2$	Anode SEI film resistance	1 - 10	[42, 48]	High
Concentration parameters	$c_{s,\max}^+$	$10^4 molm^{-3}$	Cathode maximum ionic concentration	4.8 - 5.2	[8, 38, 42, 45, 47, 48]	High
	$c_{s,\max}^-$	$10^4 molm^{-3}$	Anode maximum ionic concentration	2.9 - 3.3	[8, 38, 42, 45, 47, 48]	High
	$c_{e,0}$	$10^3 molm^{-3}$	Initial electrolyte concentration	1 - 1.2	[8, 39–41, 43, 45, 47, 48]	Medium

Table 2: Summary of parameter ranges and sensitivity of lithium-NMC-graphite cells.

which leads to a relatively large value range for some parameters. Therefore, these parameter boundaries can be used for parameter identification of almost all NMC/graphite LIB cells with small adaptions. The only parameters that require opening the cell to determine the boundaries are the electrode surface area, A, and the OCP of the electrodes. The confidence interval of the measurement is used as the boundaries of A. The opening of the cell can be avoided by implementing optical measurement methods to determine the boundaries of the geometric parameters and determining the OCP from the literature.

Each physical parameter individually influences the model output, i.e., terminal voltage, under a designed current input, which represents the sensitivity of the parameters. The consideration of insensitive parameters with large variances in the optimization problem is known to decrease the overall estimation quality substantially [55]. We have investigated the parameter sensitivity of the P2D model with the One-At-a-Time (OAT) method in our previous work [56]. The sensitivity of the parameters is mainly determined by the model structure, value range of the parameter itself, and the value of the other parameters. Therefore, all the above three factors need to be chosen to be similar to those in real-world operating conditions to investigate the sensitivity of these parameters. For all individual parameters, simulations were carried out in which the examined parameter takes up ten discrete values under uniform distribution between its value boundaries, as summarized in Table 2, and the remaining parameters are kept constant as the nominal value. The influence of different C-rates and depth of discharge (DOD) regions of the respective parameters

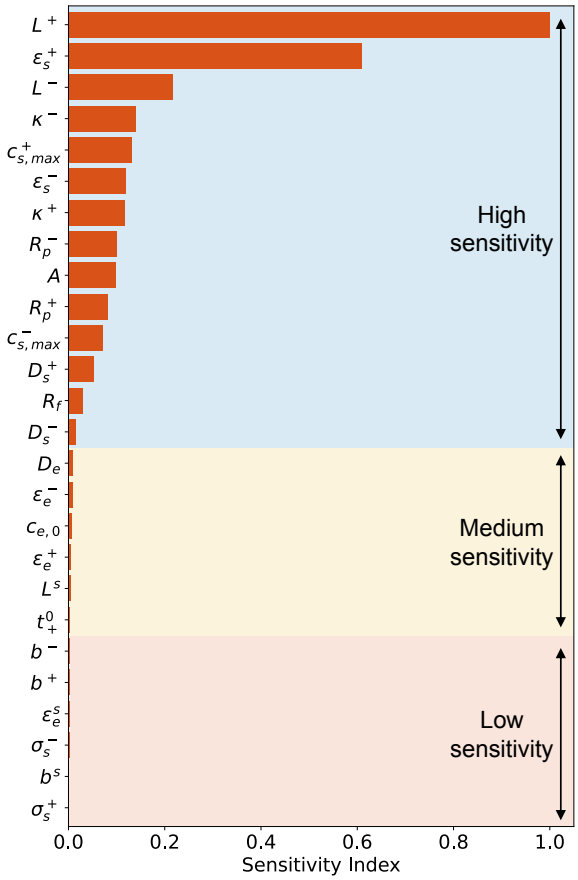

Figure 2: Summary of the parameter sensitivity related to cell terminal voltage. The parameters are categorized into three groups, i.e., high sensitivity, medium sensitivity and low sensitivity.

was tested at constant C-rate charging processes. The sensitivity of the seven capacity-related parameters varies significantly at different DOD regions due to the horizontal shift of the end-of-charge point, while the variations caused by the increase of the C-rate are moderate. In contrast, the other parameters show a significant sensitivity increase with an increase of the C-rate. In addition, the sensitivity of the parameters on real-world driving cycles was also investigated and the results are summarized in Table 2 and depicted in Fig. 2. Out of 26 parameters, 14 parameters are identified as parameters with high sensitivity for the terminal voltage considering the values of the normalized sensitivity index are over 0.01. Furthermore, six parameters are with medium sensitivity and the remaining six parameters are with low sensitivity. Besides, all capacity-related parameters, e.g., electrode surface area, A, electrode thickness, L^+ and L^-, active material volume fraction, ε_s^+ and ε_s^-, and maximum electrode ionic concentration, $c_{s,max}^+$ and $c_{s,max}^-$, are sensitive for the terminal voltage. As the cell being analyzed in this work is a high-energy cell, the electrolyte- and separator-related parameters have relatively low sensitivity, which will not be the same for the high-power

cells. The sensitivity analysis results in this work is also not universal for all cell materials and the same analysis should be carried out again when one of the three dominating factors changes. For example, the flat OCV curve in LFP and LTO cells will reduce the sensitivity of the capacity-related parameters significantly. Considering the differences in the sensitivity of the parameters, the inaccuracy of the parameters with high sensitivity can have an influence on the identification of the parameters with low sensitivity. Therefore, a multi-step parameter identification approach based on the sensitivity information is needed.

4. Data-driven parameter identification

As described in Section 3, the parameters of an EM for LIBs can be acquired through experimental measurements or be derived from physical principles based on experimental data. However, some measurements are time- and cost-intensive on the one hand and are limited in terms of accuracy on the other hand. Therefore, a novel metaheuristic algorithm will be introduced for the first time as a data-driven parameter identification method for EMs in this section.

4.1. Cuckoo search algorithm

The cuckoo search algorithm (CSA) is a metaheuristic algorithm that has been developed by Yang et al. [57, 58], inspired by the obligate brood parasitism of cuckoo. Three idealized rules were defined to simplify the breeding behavior of the cuckoo as an algorithm [59]: 1) Each cuckoo can lay only one egg at each time and dump it in a randomly selected nest. 2) The nests with high-quality eggs will be passed to the next generation. 3) The number of host nests is not adjustable. A host bird discovers an alien egg with the probability, $pa \in [0, 1]$. If a cuckoo egg is exposed, the host bird may either throw the egg away or abandon its own nest and build a new one elsewhere.

According to the above rules, the CSA was implemented as the following simple representation for the global optimization. The flowchart of the algorithm is illustrated in Fig. 3. As each egg in a nest denotes a candidate solution, the task of CSA is to generate new and potentially better solutions to replace the worse solutions in the current nest. The quality or fitness of a solution is evaluated by the objective function, which is related to the problem to be solved.

To update a new solution set according to the first rule, the global random walk for exploring the search space is implemented through the Lévy flight. For a given solution set, x_i^t with $i \in [1, n]$, where n represents the number of solution sets (nests), the next solution set x_i^{t+1} is generated by

$$x_i^{t+1} = x_i^t + \alpha \ \otimes L\acute{e}vy(\beta), \tag{1}$$

where $\alpha = \alpha_0$ (x_i^t - x_{best}^t) is the step size represented by a constant α_0 multiplied by the difference between the i^{th} solution set of the t^{th} generation, x_i^t, and the best solution so far, x_{best}^t. The symbol $\otimes$ denotes

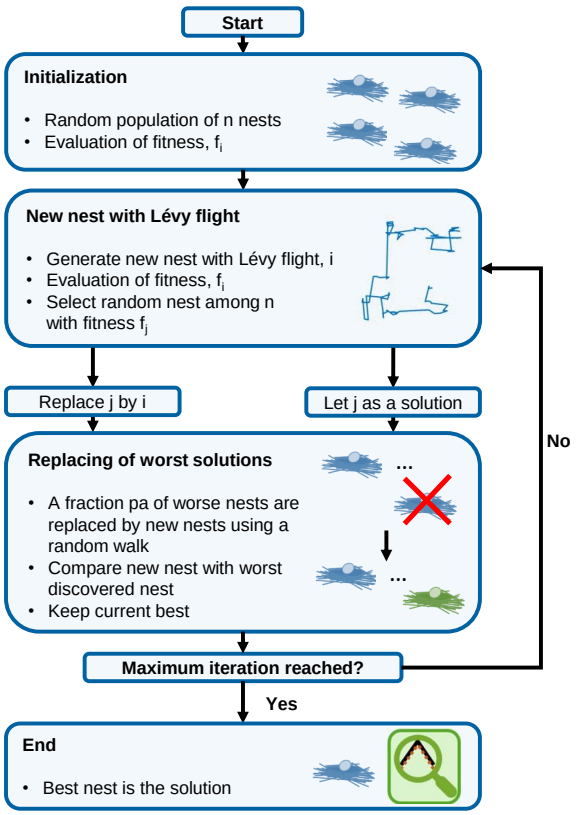

Figure 3: Flowchart of the cuckoo search algorithm.

entry-wise multiplications and $L\acute{e}vy(\beta)$ denotes the random walk step provided by Lévy flight, which is drawn from Lévy distribution as follows,

$$L\acute{e}vy(\beta) \sim \frac{u}{|v|^{\frac{1}{\beta}}}, \tag{2}$$

where the index $\beta \in (0, 2]$, $u \sim N(0, \sigma_u^2)$ and $v \sim N(0, \sigma_v^2)$ are drawn from normal distribution with

$$\sigma_u = \left\{ \frac{\Gamma(1+\beta) sin(\frac{\pi\beta}{2})}{\Gamma(\frac{(1+\beta)}{2}) \beta 2^{\frac{\beta-1}{2}}} \right\}^{\frac{1}{\beta}}, \sigma_v = 1, \tag{3}$$

where $\Gamma(\cdot)$ is the standard Gamma function. The second rule is implemented by taking the best solution set into the next iteration and the last rule is implemented by replacing the worse solution sets with new randomly generated solution sets with the probability of pa. This replacement using a local random walk can be mathematically defined as [60]

$$x_i^{t+1} = x_i^t + \alpha \ \otimes H(\epsilon - pa), \tag{4}$$

where $H(\cdot)$ is a Heaviside function used to judge whether the host bird ejects the egg and is replaced or remains in the nest, $\epsilon \in [0, 1]$ is a random number drawn from a uniform distribution and $\alpha = \epsilon(x_j^t - x_k^t)$ denotes the step size, where x_j^t and x_k^t are two different randomly selected solutions at t^{th} generation.

To summarize, CSA is a population-based algorithm, in a way similar to the PSO. However, the solution update rule based on the elitism used in CSA enables that the best solutions go to the next generation. Furthermore, the randomization via Lévy flight is a random walk that is characterized by a probability density function and has a power law tail. Another advantage of CSA is that only one parameter, pa, needs to be adjusted [61]. Therefore, although PSO and CSA on average can yield similar effectiveness or solution quality, CSA is more computationally efficient than PSO, which will be further validated for parameter identification in Section 6.1.

4.2. Multi-objective multi-step parameter identification framework

In this section, the framework for the data-driven parameter identification of the EM is provided. As depicted in Fig. 4a, the state-of-the-art experimental parameter measurement process [8, 9] for EMs is very expensive and time-consuming, as it consists of many experiments with expensive test benches and laboratory equipment. In this work, the parameters marked with blue will be identified with basic testing procedures in pre-identification experiments, e.g., quasi-open circuit voltage (qOCV) test, electrochemical impedance spectroscopy (EIS), hybrid pulse power characterization (HPPC) test, etc. The parameters marked with orange, which are usually measured with post-mortem analysis by opening the cell, will be identified with the data-driven method. Based on the sensitivity analysis results, 20 parameters with high and medium sensitivity were identified with the framework and the six parameters with low sensitivity were set as nominal values within their boundaries, as the variances of these parameters have little influence on the model performance. Especially, a novel multi-objective fitness function considering both voltage errors and capacity errors between electrodes is designed for the first time to improve the identification accuracy of the capacity-related parameters. Furthermore, a multi-step identification approach is proposed to further improve the identification accuracy of parameters with both high and medium sensitivity. Both the multi-objective and the multi-step approach are developed based on the physical understanding of the EMs and contribute to the fast and accurate identification of the parameters while maintaining their physical meaning.

4.2.1. Multi-objective fitness function

To evaluate the quality of the parameter sets during the global optimization process, fitness functions are needed and will have a significant influence on the final identification performance. In this work, the first term of the objective fitness function for parameter identification with CSA is targeted at minimizing the mean-square error (MSE) between the model-simulated voltage, $\hat{V}$, and the experimentally measured voltage, V, for a given input current as follows,

$$FF_V = \frac{1}{N_t}\sum_{1}^{N_t}(V(t) - \hat{V}(t))^2, \tag{5}$$

where N_t is the number of the data points of the dataset. With this fitness term, the global optimization algorithm aims to find the optimal parameter values by reducing the errors between the model output

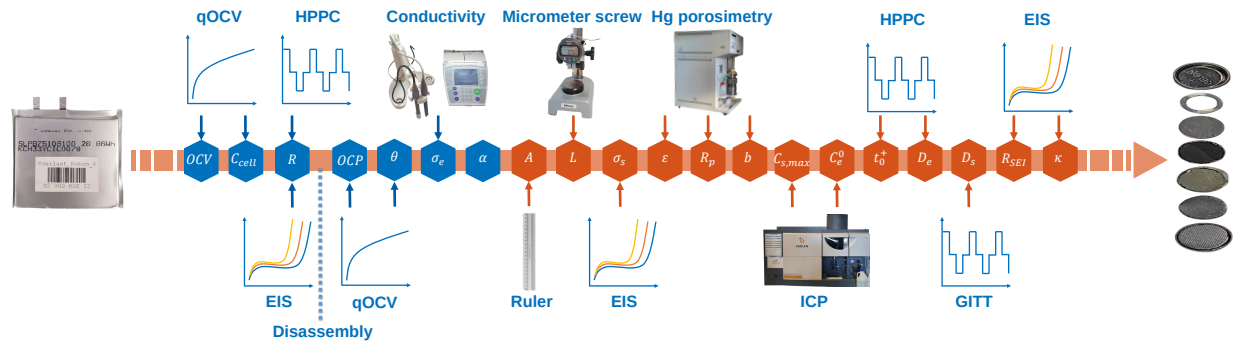

(a)

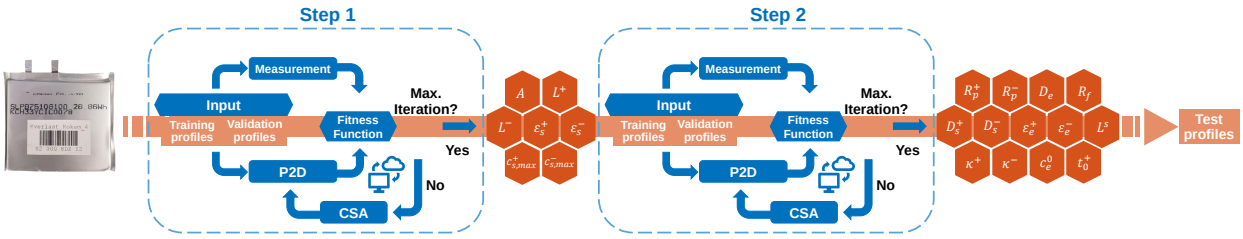

(b)

Figure 4: (a) Schematic of experiment-based parameter identification. (b) Schematic of the multi-objective multi-step data-driven identification process, together with the training process inspired by machine learning to overcome overfitting.

and the measurement. Considering that all the capacity-related parameters are with high sensitivity and influence the voltage trajectories strongly, a second fitness term is designed for the first time to constrain the error between the capacity of both electrodes, i.e., C^+ and C^-. The capacity error between cathode and anode can be calculated with the identified capacity-related parameters as follows,

$$FF_C = abs\left(\frac{A \cdot L^+ \cdot \varepsilon_s^+ \cdot F \cdot c_{s,max}^+ \cdot (\theta_0^+ - \theta_{100}^+)}{3600} - \frac{A \cdot L^- \cdot \varepsilon_s^- \cdot F \cdot c_{s,max}^- \cdot (\theta_{100}^- - \theta_0^-)}{3600}\right), \tag{6}$$

where θ_0^+, θ_{100}^+, θ_0^- and θ_{100}^- are stoichiometry values indicating the usage of cathode and anode, which can be identified with the data from the qOCV test of the full cell and electrodes. It can be noticed that we have not used the absolute error of the electrode capacity because the cell capacity is hard to be measured accurately, even under a very low C-rate. Instead, the relative capacity error reflecting the difference between the capacity of the cathode and the anode is considered. With FF_C, the identification accuracy of the capacity-related parameters can be improved significantly. In summary, the total objective fitness function consists of two fitness terms considering both voltage error and capacity error as follows,

$$FF_M = \sum_{n=1}^{N_P} w_{V_n} FF_V + w_c FF_C \tag{7}$$

where N_P is the number of the input profiles when multiple profiles are used to identify the parameters, w_{V_n} and w_C are weights for the corresponding fitness terms. The choice of the weights has a significant influence on the identification results, which can be determined based on the value of the error terms so that every term is on the same order of magnitude during the optimization process.

4.2.2. Multi-step parameter identification

The process of parameter identification using CSA starts by applying the current profiles experimentally to the LIB cell or to the numerical model. The input data thus consists of the current profiles and the resulting measured or simulated terminal voltage. In the beginning, randomized nests are initialized in the CSA, where each nest represents a random set of parameters within the value boundaries. For each nest, the voltage resulting from the current profile and the parameters of the individual nests is simulated and evaluated by the objective fitness function. Based on the fitness values, the nests are selected for whether updating or maintaining by the updating rules. After that, the new nests are re-evaluated by the model. This process is repeated until it reaches the maximum generation. Finally, the identified parameter values are acquired from the nest with minimal fitness.

Considering that the variances of the parameters with high sensitivity have a much larger influence on the voltage compared with parameters with low sensitivity, the identifiability of the parameters with low sensitivity will be hidden when they are varying with other high-sensitivity parameters at the same time. To increase the identification accuracy of the capacity-related parameters, which have high sensitivity, and reduce the influence of the identification errors of these parameters on the identification accuracy of the other parameters with relatively low sensitivity, a multi-step parameter identification approach is designed in this work. As shown in Fig. 4b, the so-called multi-step multi-objective cuckoo search algorithm (MMCSA) is divided into two identification steps. In the first step, all the parameters are identified with the multi-objective function, FF_M. In the second step, seven capacity-related parameters are set to be constant values, which are identified from the first step to reduce their influence on the identification of the low-sensitivity parameters. All the other parameters are identified further with the fitness function, FF_v, as the capacity error fitness term will not change anymore.

4.2.3. Identification process overcoming overfitting

One of the challenges of the data-driven methods is the occurrence of overfitting, which is triggered by two main reasons, especially when using a small dataset: first, the EM is not able to model the dynamics of the LIBs with 100% accuracy; second, the measurement data also contains errors. Therefore, parameter identification with the metaheuristic algorithms may lead to overfitting of the parameters when only one input profile is used, which means the further reduction of the fitness error does not denote that the identified parameters are more accurate. However, when the number of input profiles increases, the computation

burden will also increase significantly, in particular when the input profile is highly dynamic with a high sampling rate. Inspired by the training process of machine learning algorithms [62], a novel identification process to overcome overfitting is proposed in this work, as shown in Fig. 4b. The experimental data is divided into three data groups, i.e., training data, validation data and test data. In each identification step, two load profiles with low and high dynamics, e.g., discharging with constant current and multi-pulse test profile, are used as the training dataset to guide the algorithm to reduce the voltage and capacity error for 500 epochs. At the end of each training epoch, the best performance parameter set will be validated with the validation data, i.e., a driving cycle profile with high dynamics. The minimum fitness error of the validation data in the first identification step will be used as the stop criterion and the parameter set will be used as the starting parameter set in the second identification step. Similarly, the parameters will be identified further with the training dataset in the second step for another 500 epochs and the final stop criterion is based on the minimum fitness error with the validation dataset and the related parameter set is the final identification result. In the end, the identified parameters will be further tested with new load profiles, i.e., test data, for the evaluation of the identification accuracy.

5. Experimental

The battery cell we used in the experiments is a commercial high-energy NMC pouch cell of type SLPB 75106100 manufactured by Kokam Co. Ltd. As summarized in Table 3, the battery has a nominal voltage of 3.7 V and a nominal capacity of 7.5 Ah. The typical operating voltage range of the battery is from 2.7 V to 4.2 V.

Category	Specification
Manufacturer	Kokam
Type	SLPB 75106100
Nominal voltage	3.7 V
Nominal capacity	7.5 Ah
Cut-off voltages	2.7 V - 4.2 V

Table 3: Cell specifications.

5.1. Pre-identification experiments

Before the data-driven identification process, parameters from the polynomial functions of electrolyte conductivity and open circuit potential (OCP) and the stoichiometry values of the OCV were identified with experimental data. The relationship between the electrolyte conductivity and electrolyte concentration was

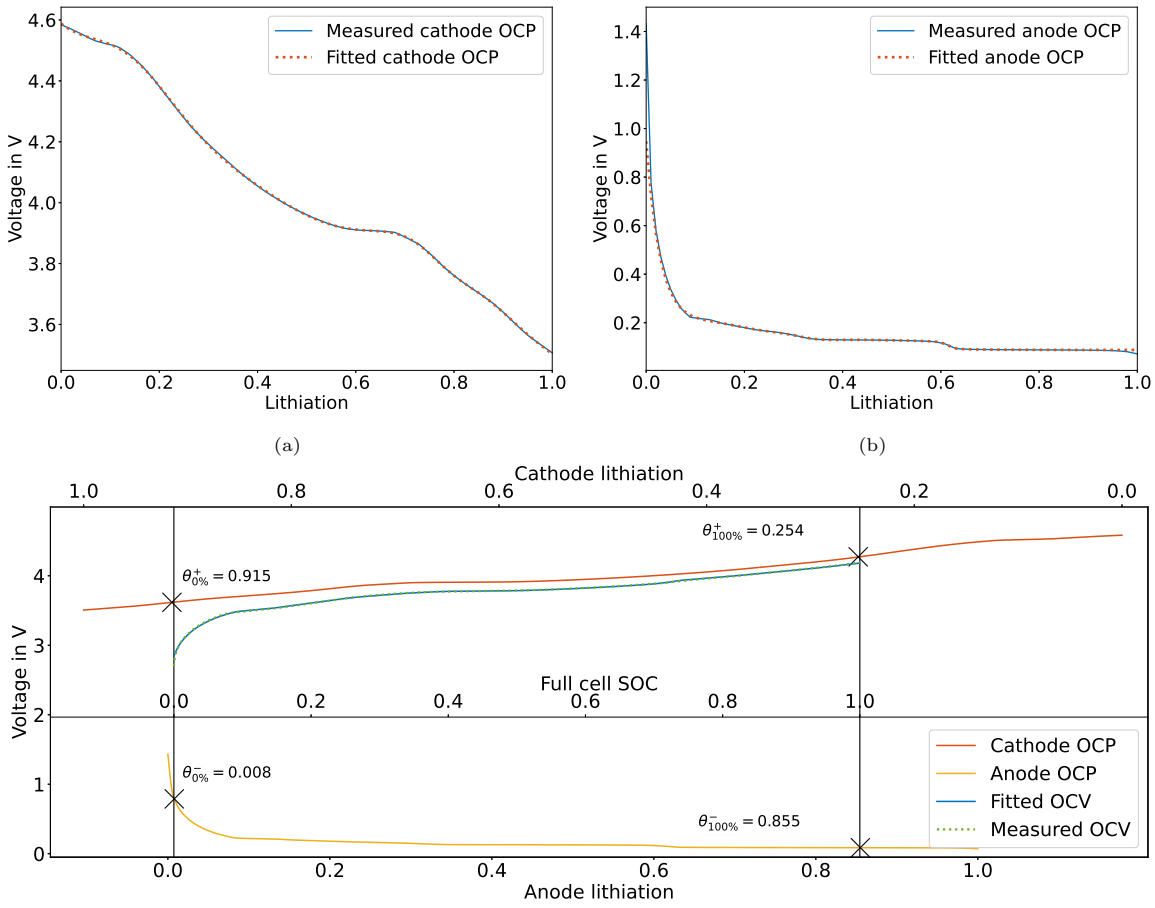

Figure 5: (a) Fitting results of the cathode OCP. (b) Fitting results of the anode OCP. (c) Cell balancing results to determine the stochiometry parameters, $\theta^+_{0\%}$, $\theta^+_{100\%}$, $\theta^-_{0\%}$, $\theta^-_{100\%}$.

measured under nitrogen atmosphere by applying an alternating current and the measurement data at 23°C [8] was fitted with a third-order polynomial using CSA as follows,

$$\sigma_e = 0.1422 + 1.877 \cdot 10^{-3} \cdot c_e - 1.3755 \cdot 10^{-6} \cdot {c_e}^2 + 2.8923 \cdot 10^{-10} \cdot {c_e}^3, \tag{8}$$

where the unit for σ_e and c_e are S/m and mol/m^3, respectively. The units for the numerical parameters are different from each other so that the units of the two sides of Eq. (8) are the same.

The OCP of both cathode and anode were measured by the coin half cells with the same electrode materials originated from the Kokam cell and the measurement data was fitted with the nonlinear functions

with the CSA as follows,

$$\begin{aligned} U^+ = 2.11 \cdot 10^{-6} + 110.52(1-\theta_p) - 1361.72(1-\theta_p)^2 + 9188.4(1-\theta_p)^3 \\ -37148.0(1-\theta_p)^4 + 94012(1-\theta_p)^5 - 150327(1-\theta_p)^6 + 147704.4(1-\theta_p)^7 \\ -81484.34(1-\theta_p)^8 + 19336.88(1-\theta_p)^9 - 0.1e^{-57824.14\theta_p^{115}} \end{aligned} \tag{9}$$

$$\begin{aligned} U^- = 0.1379 + 0.7526e^{-35.61\theta_n} - 0.0153tanh(\frac{\theta_n - 0.6142}{0.0156}) - 0.1312tanh(\frac{\theta_n - 0.3173}{0.0721}) \\ -0.1212tanh(\frac{\theta_n - 0.2120}{0.0940}) - 0.1291tanh(\frac{\theta_n - 0.4524}{0.1584}) - 0.1099tanh(\frac{\theta_n - 0.3976}{0.1596}) \\ -0.1083tanh(\frac{\theta_n - 0.4246}{0.1539}) - 0.1543tanh(\frac{\theta_n - 0.4003}{0.0985}) + 0.7192tanh(\frac{\theta_n - 0.3684}{0.1573}) \end{aligned} \tag{10}$$

where U^+ and U^- are the OCP of the cathode and anode, respectively, $\theta = c_{ss}/c_{s,max}$ represents the lithiation level of the electrode. The stoichiometry parameters, $\theta^+_{0\%}$, $\theta^+_{100\%}$, $\theta^-_{0\%}$ and $\theta^-_{100\%}$, dedicate the lithiation of cathode and anode at 0% and 100% SOC. To further determine the stoichiometry values, the OCV of the full cell was measured under constant charging and discharging with $C/20$. As shown in Fig. 5, these four parameters were identified by minimizing the error between the measured OCV and simulated OCV with the half-cell OCPs using CSA. The identified values of the stoichiometry parameters are also summarized in Table 4. Compared with the cell balancing method in Ref. [8], the root-mean-sqaure error (RMSE) between the measured OCV and fitted OCV decreases from 19.1 mV to 7.4 mV, demonstrating the high identification accuracy with the CSA. It is also worth mentioning that, the four stoichiometry parameters can also be identified together with the other physical parameters with the proposed data-driven method.

	Ref. [8]	CSA
$\theta^+_{0\%}$	0.932	0.915
$\theta^+_{100\%}$	0.260	0.254
$\theta^-_{0\%}$	0	0.008
$\theta^-_{100\%}$	0.8292	0.855
OCV RMSE	19.1 mV	7.4 mV

Table 4: Identification results of the stoichiometry parameters for the OCV using the method in Ref. [8] and CSA.

5.2. Experiments for data generation

To generate the dataset for the data-driven identification of P2D model parameters, a battery cell is connected with the test bench, which consists of a Digatron battery tester (MCFT 20-5-60 ME), a control PC, a Binder thermal chamber (Binder MK54), and a data logger. During the experiments, the battery

Load profile	Data group	Dynamic	Duration
2C discharge	Training	low	39 min
Multi-pulse test	Training	high	420 min
WLTP 1	Test	high	257 min
WLTP 2	Validation	high	463 min
WLTP 3	Test	high	931 min

Table 5: List of the experimental tests for data generation.

was placed in the thermal chamber to remain at a constant environment temperature of 25°C. The real-time measurements during tests are the input current, I, and terminal voltage, V. Furthermore, five experiments with different load profiles were carried out to generate the data for parameter identification. The test details and the categorization of the load profiles for the experiments are summarized in Table 5. Considering the short simulation time and variances in load dynamics, the measurement data under two standard testing profile, constant-current discharging test and multi-pulse test, were selected as the training data. As the aim of this work is developing a fast data-driven parameter identification approach for the application of EMs under real-world operating conditions with high dynamics, the Worldwide Harmonized Light-Duty Vehicles Test Procedure (WLTP) 2 test data was chosen as validation data to determine the stop criterion in the identification process. WLTP 1 test data and WLTP 3 test data were selected as the test dataset to evaluate the identification performance at the end of the data-driven identification process. The WLTP profiles consist of charging and discharging current pulses with various C-rates under various time duration. Compared with the constant-current discharging profile where the OCV is the dominating factor, the real-world driving cycles are more challenging for the validation of the parameter identification as both capacity-related parameters and other parameters need to be accurate enough to ensure a good model performance.

Although the sampling time used in the data logging within the experimental tests is 0.1 s, 1 s is chosen as the sampling time in the simulation to reduce the total computational time for parameter identification. The whole dataset used in this work has 126600 data points with 1 s as the sampling time. It is worth mentioning that the experimental tests summarized in Table 5 are only one example of the possible tests for data generation and other tests can also be chosen. As one of the highlights in this work is to avoid the overfitting problem with the machine learning-inspired identification process when a small dataset is available, only two profiles are used as training profiles. A larger number of training profiles can also be used to further increase the identification accuracy but with a significant increase of the computational time. Although sparser data can also be chosen, it is strongly suggested that at least two datasets with different

dynamics should be used in the training process, one dataset for the validation process and one dataset for the test process, to avoid the overfitting of the parameters. Incomplete or fragmented data can also be used if the dataset can cover the main SOC range and with different load dynamics, which are very common in the real operation condition.

6. Results and discussion

In this section, the proposed data-driven parameter identification method is validated not only with a virtual cell with known parameters numerically but also with a commercial cell experimentally. Different benchmarks considering algorithm, fitness function and identification framework are used to highlight the outstanding performance of the proposed method. Last but not least, the model performance with the experimental identification method is also provided, discussed and compared with the model performance with data-driven identified parameters.

6.1. Numerical validation

As the real values of the P2D model parameters are not accessible and even the invasive experimental measurements by opening the cell cannot guarantee the identification with 100% accuracy, we first validate the data-driven parameter identification framework numerically with a virtual cell with known parameters. The virtual cell consists of the same P2D model used in the identification process, as introduced in Section 2, and the real values of the parameters were chosen randomly within the predefined parameter boundaries, as summarized in Table 2. The virtual cell was tested under the load profiles, as listed in Table 5, to generate the training dataset, validation dataset and test dataset. The current and simulated voltage of the virtual cell were used as the input data for the data-driven parameter identification with the MMCSA and other algorithm benchmarks.

6.1.1. Comparative study with particle swarm optimization

As the PSO has already shown notable advantages compared with GA in parameter identification for P2D models in the literature, PSO is used as a benchmark in this work to highlight the fast convergence and high identification efficiency of the CSA. To compare the algorithm performance fairly, the fitness function in Eq. (5) for both PSO and CSA was set to be the same and the hyperparameters of the PSO and CSA were also tuned with trial-and-error procedures to guarantee the best performance of each algorithm.

Due to the algorithm difference, the parameter sets are updated and simulated in each identification iteration once with PSO but twice with CSA. Therefore, the simulation number rather than the iteration number can represent the real computation time of the algorithm, which is then used as the index for a fair comparison. The development of the fitness values for 2000 simulations during the parameter identification with PSO and CSA are shown in Fig. 6a. The convergence speed of the CSA is much faster than that of the

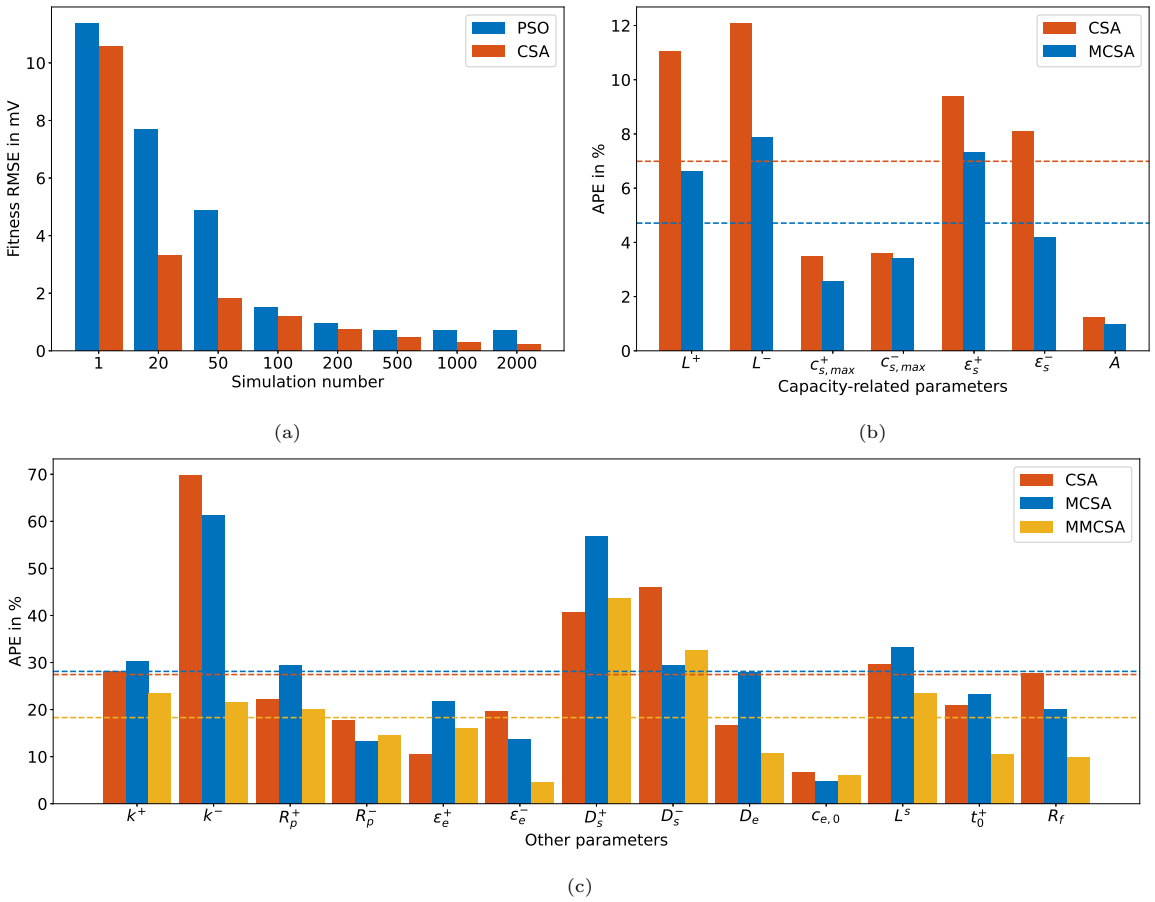

Figure 6: Numerical validation results. (a) The fitness value, RMSE, of the parameter identification using PSO and CSA for the first 2000 simulations. Mean percentage error of (b) capacity-related parameters and (c) other parameters identified with CSA, MCSA and MMCSA within ten numerical identifications. The dash lines represent the mean value of the APEs.

PSO. Furthermore, the fitness RMSE of the PSO remains almost unchanged after 500 simulations, while the fitness RMSE of the CSA continues decreasing, indicating the higher ability of the CSA in finding the global optimization point in such a complex nonlinear system compared with the PSO. The final fitness RMSE of the parameter sets under PSO and CSA is 0.721 mV and 0.215 mV, respectively, indicating that CSA can identify the parameters more efficiently. The higher convergence speed and better effectiveness in parameter identification of nonlinear systems with the CSA compared to PSO are mainly due to the following two reasons. First, there are fewer hyperparameters in CSA that need to be optimized to achieve a high performance of the algorithm, making it easier to select the hyperparameters. Second, the combination of the local optimization by the random walk and the global optimization by the random steps via Lévy flights is a very efficient method to search the global optimization solution in the search space. The comparison results with the PSO further highlights the high convergence speed and efficiency of the CSA in parameter identification for the P2D model.

Parameter	Unit	Virtual value	CSA APE [%]	MCSA APE [%]	MMCSA APE [%]
High sensitivity					
L^+	μm	54.6	11.07	6.62	6.65
L^-	μm	60.6	12.08	7.87	13.67
$c^+_{s,max}$	$\mathrm{mol\,m^{-3}}$	50778	3.47	2.57	2.07
$c^-_{s,max}$	$\mathrm{mol\,m^{-3}}$	32095	3.58	3.43	3.71
ε^+_s	-	0.4322	9.41	7.33	7.09
ε^-_s	-	0.4815	8.11	4.19	8.64
A	$\mathrm{m^2}$	0.3828	1.22	0.98	0.82
κ^+	$\mathrm{m^{2.5}s^{-1}mol^{-0.5}}$	6.82×10^{-11}	28.09	30.28	23.54
κ^-	$\mathrm{m^{2.5}s^{-1}mol^{-0.5}}$	9.19×10^{-11}	69.77	61.24	21.65
R^+_p	μm	7.08	22.18	29.51	20.16
R^-_p	μm	8.71	17.85	13.39	14.66
D^+_s	$\mathrm{m^2/s}$	5.04×10^{-14}	40.66	56.76	43.68
D^-_s	$\mathrm{m^2/s}$	2.98×10^{-14}	46.03	29.32	32.71
R_f	$\Omega\mathrm{m^2}$	0.0081	27.82	20.09	9.98
Medium sensitivity					
ε^+_e	-	0.3867	10.61	21.75	16.03
ε^-_e	-	0.4373	19.55	13.81	4.64
D_e	$\mathrm{m^2/s}$	1.77×10^{-10}	16.77	27.91	10.83
$c_{e,0}$	$\mathrm{mol\,m^{-3}}$	1133	6.75	4.79	5.95
L^s	μm	23.1	29.73	33.34	23.48
t^0_+		0.2744	20.95	23.33	10.59
C^+	Ah	8.138	0.038	0.005	0.017
C^-	Ah	8.138	0.118	0.004	0.016

Table 6: Summary of the parameter identification results with CSA, MCSA and MMCSA.

6.1.2. Validation of the multi-objective multi-step approach

To verify the improvement of the parameter identification accuracy with the multi-objective multi-step approach, two identification approaches based on CSA were further implemented as benchmarks. The first benchmark algorithm is the CSA with Eq. (5) as the fitness function, where only the voltage error between the measurement and model output is considered, which corresponds to the approach in most of the literature. The second benchmark algorithm is the multi-objective CSA (MCSA) with Eq. (7) as fitness function but without the second identification step to further improve the identification accuracy of the parameters with medium sensitivity.

The final parameter identification results with CSA, MCSA and MMCSA, are summarized in Table 6, where the absolute percentage errors (APEs) of the parameters are highlighted for all the algorithms. It is clear that most of the parameters with high sensitivity can be identified with better accuracy with MCSA compared to CSA, which is due to the multi-objective function, which further reduces the identification errors of the capacity-related parameters. Furthermore, most of the parameters with medium sensitivity

Parameter	Unit	CSA	MCSA	MMCSA
MPE_H	%	21.52	19.54	14.93
MPE_M	%	17.39	20.82	11.92
MPE_{total}	%	20.28	19.9	14.03
Voltage $RMSE$	mV	0.095	0.104	0.068

Table 7: Comparision results with CSA, MCSA and MMCSA.

can be identified with higher accuracy with MMCSA compared with MCSA, benefiting from the second identification step where some of the high-sensitivity parameters remain constant and therefore reduce their negative influence on the identification of the other parameters. As a result of the fitness term in Eq. (6), MCSA and MMCSA not only show much lower capacity identification errors for both cathode and anode, compared with CSA but also approach to the same value, which is critical for reproducing the cell dynamics. In Table 7, the mean APE of all the high-sensitivity parameters, MPE_H, the mean APE of all the medium-sensitivity parameters, MPE_M, the mean APE of all the parameters, MPE_{total}, and the voltage RMSE of all the algorithms are summarized. It can be seen that MMCSA has achieved the lowest errors in all the performance indexes, which further highlights the outstanding ability of the proposed algorithm in parameter identification for the P2D model.

Considering the randomness of the metaheuristic algorithms, ten simulations were performed with CSA, MCSA and MMCSA to further compare their performance and mitigate the influence of the uncertainty of each simulation. In Fig. 6b, the APE of the capacity-related parameters are shown for CSA and MCSA. As expected, MCSA has reduced the mean APE of the capacity-related parameters by 32.9% compared with CSA. The APE of all the other parameters, together with the MPEs for CSA, MCSA and MMCSA, are further depicted in Fig. 6c. For the other parameters, the advantage of the MMCSA algorithm is highly noticeable. As CSA and MCSA don't have a second identification step, the MPEs of the other parameters are much higher than those of the MMCSA. MMCSA further reduces the identification error of the other parameters by 34.9%, which leads to a lower voltage error and demonstrates the significance of the multi-step identification approach.

6.2. Experimental validation

After the numerical evaluation of the performance of the data-driven parameter identification algorithms, the MMCSA was used to identify the parameters of the Kokam cell, as described in Section 5, based on the measurement data. For this purpose, the framework described in Section 4.2 was used and the test data with different load profiles were divided into three groups, as summarized in Table 5. The data of the 2C discharge and the multi-pulse test were used as training data. The data of the WLTP 2 was used as validation data, whereas WLTP 1 and WLTP 3 were used as test data.

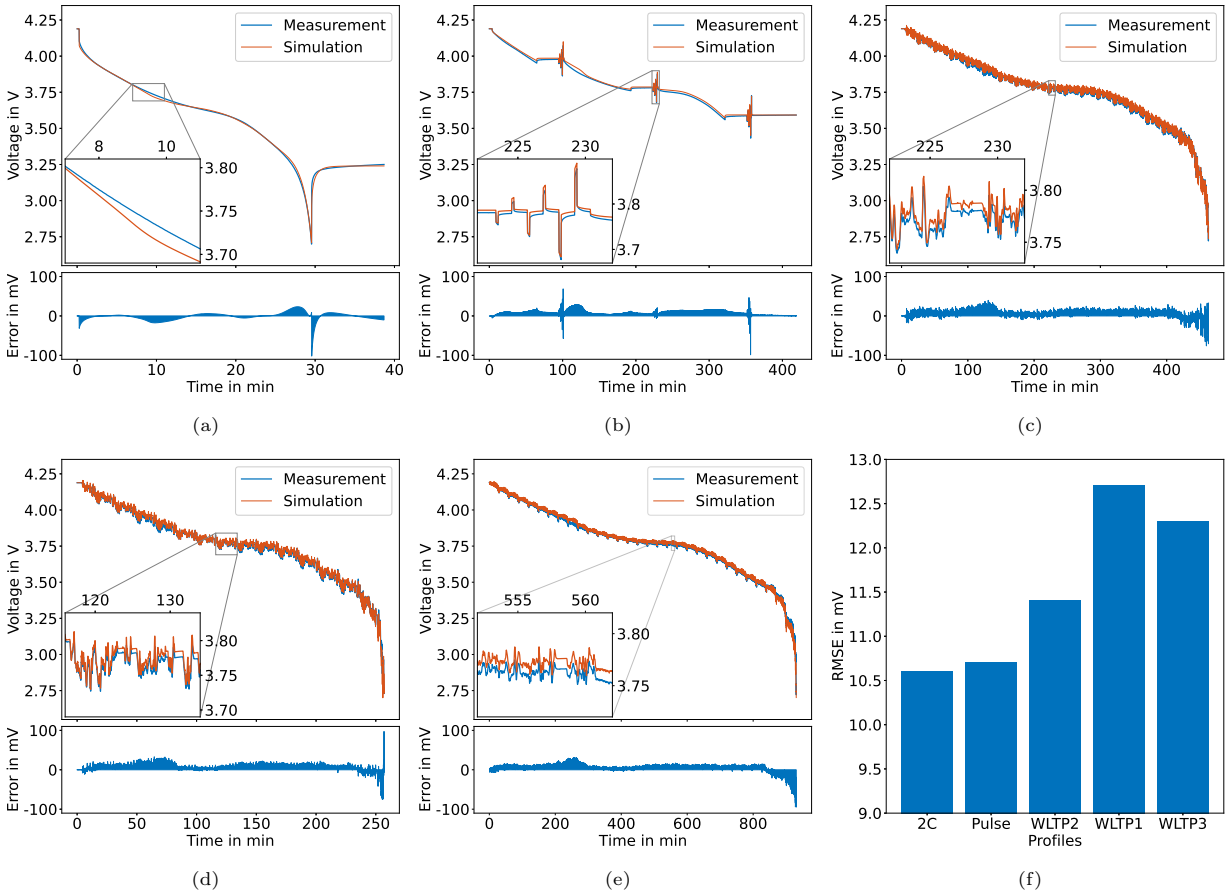

Figure 7: Experimental validation results. Model performance with the training dataset (a) 2C discharge and (b) multi-pulse test. Model performance with the validation dataset (c) WLTP 2, test dataset (d) WLTP 1 and (e) WLTP 3. (f) The RMSEs of the P2D model in all the datasets.

For the data-driven parameter identification, 500 iterations each were performed for the first and second steps. For each iteration, 25 nests were considered. The simulations were executed with an Intel Xeon Platinum 8160 processor with 26 cores and both steps of the MMCSA took about 15 hours. As introduced in Section 4.2, the weight tuning in the multi-objective fitness function is a nontrivial task and needs to balance the convergence of each fitness term considering their magnitudes. During the simulations, it was found that a stronger weighting of the 2C discharge profile in both steps led to significantly lower overfitting of the training data and thus continuously reduced the voltage MSE of the validation profile with the iterations. In contrast, a stronger weighting of the pulse profile resulted in significant overfitting, which is shown by the high voltage error under the WLTP 2 profile. The simulations showed that a weighting of $w_{V1} = 0.8$ for the 2C profile, $w_{V2} = 0.2$ for the pulse profile in both steps and additionally $w_c = 0.0005$ for the capacity in the first step provided the best results.

Fig. 7 shows the results of the data-driven parameter identification with MMCSA under different load

profiles with both low and high dynamics. It can be seen that the data-driven parameter identification with MMCSA provides a parameter set that performs well with the training data as well as with the validation data and test data. While the RMSEs of the training profiles are slightly above 10 mV, the validation profiles with 11.4 mV RMSE and the test profiles with less than 13 mV RMSEs both achieve a good fitting result over the whole profile, demonstrating the high generalization ability of the multi-objective multi-step identification approach. The relatively larger voltage errors at low SOC range and high currents are mainly due to the OCV fitting error, model inaccuracies and measurement errors.

To further compare the identification accuracy of the proposed data-driven method with the state-of-the-art experimental method, the parameters determined for the same cell with an invasive experimental method by opening the cell in the previous work of our lab [8, 9] were used as a benchmark. The parameter values of the experimental and data-driven method are summarized in Table 8. Although several parameters have shown differences in two parameter sets, the magnitudes of the identified parameters are the same as those of the measured parameters, which highlights the physical meaning of the identified parameters. As the measurement of the parameters with invasive experimental methods cannot avoid measurement errors, the variances between the two parameter set in Table 8 cannot be used as the metric to evaluate the performance of the proposed data-driven method. The electrode capacities calculated with the parameters identified by the MMCSA are 7.5202 Ah and 7.5236 Ah for cathode and anode, respectively, which shows a high consistency and also corresponds to the cell capacity specified by the manufacturer. In contrast, the capacity of the cathode and anode calculated with the parameters measured by the invasive experimental method has shown a much larger difference, which also differs from the capacity value in the cell specifications.

The performance of the experimental and data-driven parameter identification methods are further compared under a low dynamic load profile and a high dynamic load profile, as shown in Fig. 8, and the voltage and capacity errors are also summarized in Table 9. It can be observed that the data-driven method performed much better than the invasive experimental method considering the voltage error between the measurement and the model output, which is contributed by the high accuracy of both the capacity-related and impedance-related parameters. The voltage errors of the model with the experimentally measured parameters, especially in the lower SOC range, are significantly higher than those with the data-driven identified parameters in both constant-current discharging and WLTP profiles. While the voltage MAEs of the data-driven method under 2C discharge and WLTP 1 are 6.4 mV and 10.6 mV, respectively, the voltage MAEs of the experimental identification method are 45.7 mV and 24.7 mV for the same profiles. The capacity error of the data-driven method is 3.4 mAh, which is only 4.6% of that of the experimental identification. Therefore, it can be concluded that the data-driven parameter identification approach with MMCSA not only saves time and cost of the whole identification process but also provides P2D model parameters that provide a significantly lower model error compared with state-of-the-art invasive experimental identification methods by opening the cell. The high uncertainty of the capacity-related parameters may

Parameter	Sensitivity	Unit	Measurement	MMCSA
L^+	High	μm	54.5	61.04
L^-	High	μm	73.7	66.39
$c^+_{s,max}$	High	$\mathrm{mol\,m^{-3}}$	48580	48839
$c^-_{s,max}$	High	$\mathrm{mol\,m^{-3}}$	31920	31410
ε^+_s	High	-	0.4083	0.3661
ε^-_s	High	-	0.3724	0.4090
A	High	$\mathrm{m^2}$	0.3949	0.3887
κ^+	High	$\mathrm{m^{2.5}s^{-1}mol^{-0.5}}$	3.0×10^{-11}	4.4×10^{-11}
κ^-	High	$\mathrm{m^{2.5}s^{-1}mol^{-0.5}}$	11.1×10^{-11}	3.5×10^{-11}
R^+_p	High	μm	6.49	6.53
R^-_p	High	μm	13.7	8.55
D^+_s	High	$\mathrm{m^2/s}$	9.00×10^{-14}	9.49×10^{-14}
D^-_s	High	$\mathrm{m^2/s}$	10.00×10^{-14}	9.97×10^{-14}
R_f	High	$\Omega\mathrm{m^2}$	0	0.0001
ε^+_e	Medium	-	0.296	0.3770
ε^-_e	Medium	-	0.329	0.2301
D_e	Medium	$\mathrm{m^2/s}$	2.40×10^{-10}	6.82×10^{-10}
$c_{e,0}$	Medium	$\mathrm{mol\,m^{-3}}$	1000	1137
L^s	Medium	μm	19.0	11.37
t^0_+	Medium	-	0.2600	0.2300
C^+	-	Ah	7.6886	7.5202
C^-	-	Ah	7.6144	7.5236

Table 8: Summary of the values of the identified parameters using the experimental measurement and the MMCSA.

	2C discharge		WLTP 1	
	Experimental	MMCSA	Experimental	MMCSA
Voltage RMSE	50.1 mV	9 mV	31.4 mV	12.7 mV
Voltage MAE	45.7 mV	6.4 mV	24.7 mV	10.6 mV
Δ capacity	74.2 mAh	3.4 mAh	74.2 mAh	3.4 mAh

Table 9: Comparison of the voltage errors and capacity error of the experimental identification method and the data-driven identification method with MMCSA.

lead to over-charging or over-discharging of the battery cells with a wrong SOC estimation. Furthermore, the identification errors in impedance-related parameters can not only lead to errors in state estimation but also increase the error in power prediction of LIBs, which may affect the energy management [63–66] or cause safety problems.

6.3. Future work and applications

In the future, we aim to expand the scope of this work in various directions, one of which is expanding the identification ability of the framework for electrochemical-thermal models by further considering the

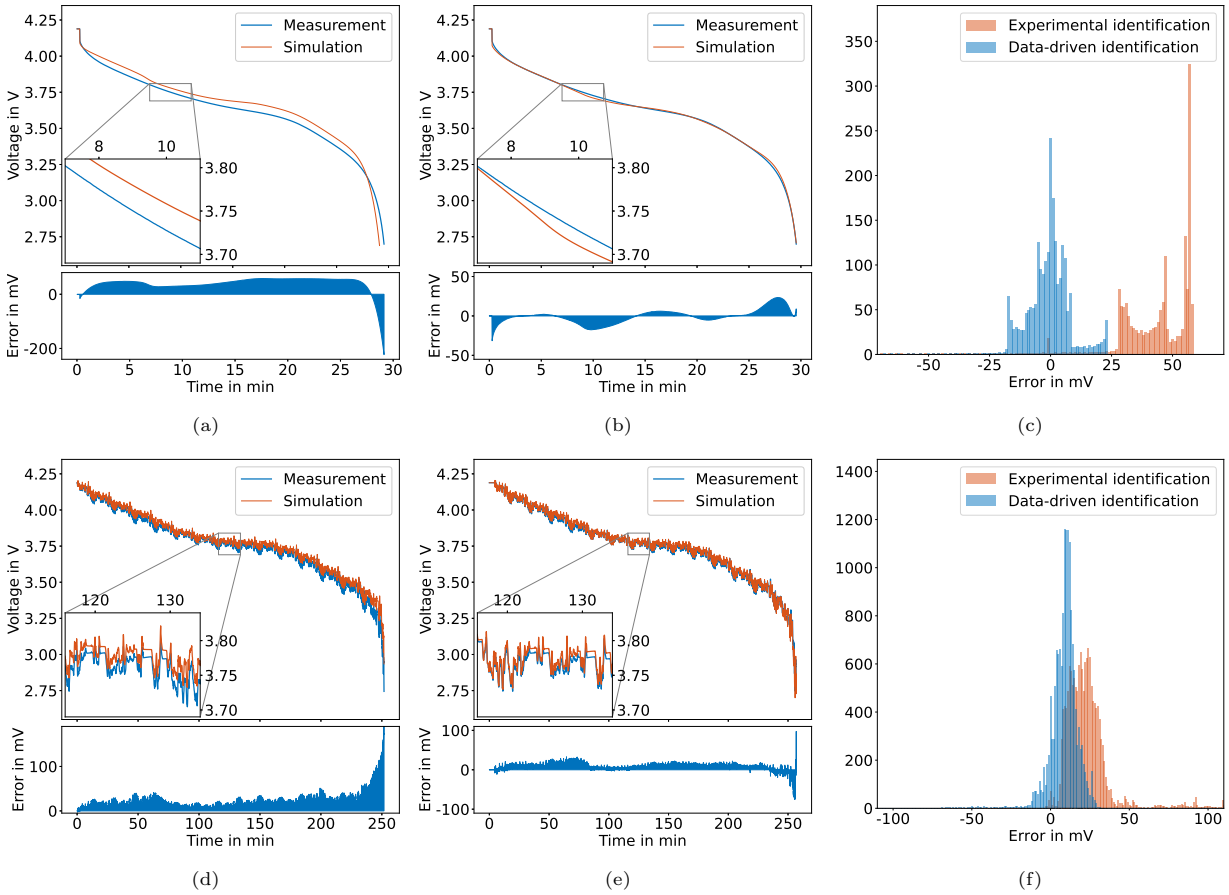

Figure 8: Comparative study between the experimental and data-driven parameter identifications. Performance of the model under 2C discharge with the parameters identified with (a) the invasive experimental method and (b) the data-driven method. (c) Error distributions of the invasive experimental and data-driven parameter identification results under 2C discharge. Performance of the model under WLTP 1 with the parameters identified with (d) the invasive experimental method and (e) the data-driven method. (f) Error distributions of the invasive experimental and data-driven parameter identification results under WLTP 1.

identification of thermal parameters. A major step would be analyzing the sensitivity of the thermal and physical parameters to voltage and temperature measurement with a variance-based global sensitivity analysis method, further increasing the sensitivity analysis accuracy. To identify the parameters, which are valid for a large operating temperature range, the battery testing procedures need to be expanded for tests under various temperatures.

Another key expansion to the framework is investigating identification methods for the aging-related parameters of EMs under operation. First, electrode level aging mechanisms can be understood by identifying the parameters for each electrode and the contributions of loss of lithium inventory (LLI) and loss of active material (LAM) to battery aging can be clarified by identifying the stoichiometry parameters of the cell

balancing online. The updated model parameters can be sent to the battery systems in EVs by Over-the-Air-Update technology [67], guaranteeing the reliability of the EM-based battery management functions, such as fast charging, over the whole lifetime of EVs.

7. Conclusions

This work aims to develop a parameter identification framework that is suitable for fast and accurate identification of physical parameters of electrochemical models under real-world operation. The proposed data-driven parameter identification framework not only shows significant performance improvement compared with the other data-driven methods but also shows a higher identification accuracy compared with the state-of-the-art experimental identification method. Several highlights of the framework are given below.

- Identifies 26 parameters of an electrochemical model only based on voltage and current measurement and overcomes the overfitting problem by a novel identification process inspired by the training process in machine learning.
- Multi-objective fitness functions are considered, improving the identification accuracy of capacity-related parameters significantly, which is essential for a low voltage error between the model and the cell.
- Multi-step identification procedure reduces the negative influences of the identification of the high-sensitivity parameters on the identification of the low-sensitivity parameters, therefore, increases the identifiability and reduces the identification errors.
- Cuckoo search algorithm identifies the parameters more accurately and with a faster convergence speed compared with other metaheuristic algorithms, e.g., particle swarm optimization.
- Compared with the experimental identification method, the proposed data-driven approach reduces 82.0% and 59.6% of the voltage error under low and high load dynamics, respectively, and reduces 95.4% capacity error between two electrodes.

At the time of review for this work, no comparable work was found in the same domain, which implements a cuckoo search algorithm under a multi-objective multi-step framework for the identification of parameters for lithium-ion electrochemical models. The validation of the identification framework not only with a virtual cell numerically and with a commercial cell experimentally are conducted to show the viability of acceptance of data-driven methods in future battery research.

Acknowledgment

This work has received funding from the European Union's Horizon 2020 research and innovation program under the grant "Electric Vehicle Enhanced Range, Lifetime And Safety Through INGenious battery management" (EVERLASTING-713771). Part of the work was done within the research project "Model2life" (03XP0334) funded by the German Federal Ministry of Education and Research (BMBF). We would like to thank D. Luder for the review and the discussions and C. Rahe for the photos of the lab devices.

References

[1] R. Schmuch, R. Wagner, G. Hörpel, T. Placke, M. Winter, Performance and cost of materials for lithium-based rechargeable automotive batteries, Nature Energy 3 (4) (2018) 267–278. doi:10.1038/s41560-018-0107-2.

[2] W. Li, Y. Fan, F. Ringbeck, D. Jöst, X. Han, M. Ouyang, D. U. Sauer, Electrochemical model-based state estimation for lithium-ion batteries with adaptive unscented Kalman filter, Journal of Power Sources 476 (2020) 228534. doi:10.1016/j.jpowsour.2020.228534.

[3] W. Li, D. W. Limoge, J. Zhang, D. U. Sauer, A. M. Annaswamy, Estimation of potentials in lithium-ion batteries using machine learning models, IEEE Transactions on Control Systems Technology (2021) 1–16doi:10.1109/TCST.2021.3071643.

[4] W. Li, J. Zhang, F. Ringbeck, D. Jöst, L. Zhang, Z. Wei, D. U. Sauer, Physics-informed neural networks for electrode-level state estimation in lithium-ion batteries, Journal of Power Sources 506 (5) (2021) 230034. doi:10.1016/j.jpowsour.2021.230034.

[5] J. Li, D. Wang, L. Deng, Z. Cui, C. Lyu, L. Wang, M. Pecht, Aging modes analysis and physical parameter identification based on a simplified electrochemical model for lithium-ion batteries, Journal of Energy Storage 31 (6) (2020) 101538. doi:10.1016/j.est.2020.101538.

[6] W. Li, Y. Fan, F. Ringbeck, D. Jöst, D. U. Sauer, Unlocking electrochemical model-based online power prediction for lithium-ion batteries via Gaussian process regression, Applied Energy (2021).

[7] F. Ringbeck, M. Garbade, D. U. Sauer, Uncertainty-aware state estimation for electrochemical model-based fast charging control of lithium-ion batteries, Journal of Power Sources 470 (2020) 228221. doi:10.1016/j.jpowsour.2020.228221.

[8] M. Ecker, T. K. D. Tran, P. Dechent, S. Käbitz, A. Warnecke, D. U. Sauer, Parameterization of a physico-chemical model of a lithium-ion battery: I. determination of parameters, Journal of The Electrochemical Society 162 (9) (2015) A1836–A1848. doi:10.1149/2.0551509jes.

[9] M. Ecker, S. Käbitz, I. Laresgoiti, D. U. Sauer, Parameterization of a physico-chemical model of a lithium-ion battery: II. model validation, Journal of The Electrochemical Society 162 (9) (2015) A1849–A1857. doi:10.1149/2.0541509jes.

[10] J. Schmalstieg, C. Rahe, M. Ecker, D. U. Sauer, Full cell parameterization of a high-power lithium-ion battery for a physico-chemical model: Part I. Physical and electrochemical parameters, Journal of The Electrochemical Society 165 (16) (2018) A3799–A3810. doi:10.1149/2.0321816jes.

[11] J. Schmalstieg, D. U. Sauer, Full cell parameterization of a high-power lithium-ion battery for a physico-chemical model: Part II. Thermal parameters and validation, Journal of The Electrochemical Society 165 (16) (2018) A3811–A3819. doi:10.1149/2.0331816jes.

[12] A. Sharma, H. K. Fathy, Fisher identifiability analysis for a periodically-excited equivalent-circuit lithium-ion battery model, in: American Control Conference (ACC), 2014, IEEE, Piscataway, NJ, 2014, pp. 274–280. doi:10.1109/ACC.2014.6859360.

[13] V. Boovaragavan, S. Harinipriya, V. R. Subramanian, Towards real-time (milliseconds) parameter estimation of lithium-ion batteries using reformulated physics-based models, Journal of Power Sources 183 (1) (2008) 361–365. doi:10.1016/j.jpowsour.2008.04.077.

[14] V. Ramadesigan, K. Chen, N. A. Burns, V. Boovaragavan, R. D. Braatz, V. R. Subramanian, Parameter estimation and capacity fade analysis of lithium-ion batteries using reformulated models, Journal of The Electrochemical Society 158 (9) (2011) A1048. doi:10.1149/1.3609926.

[15] S. Santhanagopalan, Q. Guo, R. E. White, Parameter estimation and model discrimination for a lithium-ion cell, Journal of The Electrochemical Society 154 (3) (2007) A198. doi:10.1149/1.2422896.

[16] Z. Deng, H. Deng, L. Yang, Y. Cai, X. Zhao, Implementation of reduced-order physics-based model and multi-parameters identification strategy for lithium-ion battery, Energy 138 (2017) 509–519. doi:10.1016/j.energy.2017.07.069.

[17] A. P. Schmidt, M. Bitzer, Á. W. Imre, L. Guzzella, Experiment-driven electrochemical modeling and systematic parameterization for a lithium-ion battery cell, Journal of Power Sources 195 (15) (2010) 5071–5080. doi:10.1016/j.jpowsour.2010.02.029.

[18] O. Bozorg-Haddad, M. Solgi, H. A. Loáiciga (Eds.), Meta-Heuristic and Evolutionary Algorithms for Engineering Optimization, John Wiley & Sons, Inc, Hoboken, NJ, USA, 2017. doi:10.1002/9781119387053.

[19] J. C. Forman, S. J. Moura, J. L. Stein, H. K. Fathy, Genetic identification and fisher identifiability analysis of the doyle–fuller–newman model from experimental cycling of a lifepo4 cell, Journal of Power Sources 210 (2012) 263–275. doi:10.1016/j.jpowsour.2012.03.009.

[20] A. Jokar, B. Rajabloo, M. Désilets, M. Lacroix, An inverse method for estimating the electrochemical parameters of lithium-ion batteries, Journal of The Electrochemical Society 163 (14) (2016) A2876–A2886. doi:10.1149/2.0191614jes.

[21] L. Zhang, C. Lyu, L. Wang, J. Zheng, W. Luo, K. Ma, Parallelized genetic identification of the thermal-electrochemical model for lithium-ion battery, Advances in Mechanical Engineering 5 (2013) 754653. doi:10.1155/2013/754653.

[22] L. Zhang, C. Lyu, G. Hinds, L. Wang, W. Luo, J. Zheng, K. Ma, Parameter sensitivity analysis of cylindrical LiFePO4 battery performance using multi-physics modeling, Journal of The Electrochemical Society 161 (5) (2014) A762–A776. doi:10.1149/2.048405jes.

[23] J. Li, L. Zou, F. Tian, X. Dong, Z. Zou, H. Yang, Parameter identification of lithium-ion batteries model to predict discharge behaviors using heuristic algorithm, Journal of The Electrochemical Society 163 (8) (2016) A1646–A1652. doi:10.1149/2.0861608jes.

[24] H. Pang, L. Mou, L. Guo, F. Zhang, Parameter identification and systematic validation of an enhanced single-particle model with aging degradation physics for li-ion batteries, Electrochimica Acta 307 (2019) 474–487. doi:10.1016/j.electacta.2019.03.199.

[25] J. Li, D. Wang, L. Deng, Z. Cui, C. Lyu, L. Wang, M. Pecht, Aging modes analysis and physical parameter identification based on a simplified electrochemical model for lithium-ion batteries, Journal of Energy Storage 31 (2020) 101538. doi:10.1016/j.est.2020.101538.

[26] J. Li, L. Wang, C. Lyu, E. Liu, Y. Xing, M. Pecht, A parameter estimation method for a simplified electrochemical model for li-ion batteries, Electrochimica Acta 275 (2018) 50–58. doi:10.1016/j.electacta.2018.04.098.

[27] Y. Y. Choi, S. Kim, S. Kim, J.-I. Choi, Multiple parameter identification using genetic algorithm in vanadium redox flow batteries, Journal of Power Sources 450 (2020) 227684. doi:10.1016/j.jpowsour.2019.227684.

[28] R. Ahmed, M. El Sayed, I. Arasaratnam, J. Tjong, S. Habibi, Reduced-order electrochemical model parameters identification and soc estimation for healthy and aged li-ion batteries part i: Parameterization model development for healthy batteries, IEEE Journal of Emerging and Selected Topics in Power Electronics 2 (3) (2014) 659–677. doi:10.1109/JESTPE.2014.2331059.

[29] W. Li, M. Rentemeister, J. Badeda, D. Jöst, D. Schulte, D. U. Sauer, Digital twin for battery systems: Cloud battery

management system with online state-of-charge and state-of-health estimation, Journal of Energy Storage 30 (2020) 101557. doi:10.1016/j.est.2020.101557.

[30] M. A. Rahman, S. Anwar, A. Izadian, Electrochemical model parameter identification of a lithium-ion battery using particle swarm optimization method, Journal of Power Sources 307 (2016) 86–97. doi:10.1016/j.jpowsour.2015.12.083.

[31] X. Yang, L. Chen, X. Xu, W. Wang, Q. Xu, Y. Lin, Z. Zhou, Parameter identification of electrochemical model for vehicular lithium-ion battery based on particle swarm optimization, Energies 10 (11) (2017) 1811. doi:10.3390/en10111811.

[32] Z. Chu, R. Jobman, A. Rodríguez, G. L. Plett, M. S. Trimboli, X. Feng, M. Ouyang, A control-oriented electrochemical model for lithium-ion battery. Part II: Parameter identification based on reference electrode, Journal of Energy Storage 27 (2020) 101101. doi:10.1016/j.est.2019.101101.

[33] G. Fan, Systematic parameter identification of a control-oriented electrochemical battery model and its application for state of charge estimation at various operating conditions, Journal of Power Sources 470 (2020) 228153. doi:10.1016/j.jpowsour.2020.228153.

[34] M. Doyle, T. F. Fuller, J. Newman, Modeling of galvanostatic charge and discharge of the lithium/polymer/insertion cell, Journal of The Electrochemical Society 140 (6) (1993) 1526. doi:10.1149/1.2221597.

[35] N. A. Chaturvedi, R. Klein, J. Christensen, J. Ahmed, A. Kojic, Algorithms for advanced battery-management systems, IEEE Control Systems 30 (3) (2010) 49–68. doi:10.1109/MCS.2010.936293.

[36] V. R. Subramanian, V. Boovaragavan, V. Ramadesigan, M. Arabandi, Mathematical model reformulation for lithium-ion battery simulations: Galvanostatic boundary conditions, Journal of The Electrochemical Society 156 (4) (2009) A260. doi:10.1149/1.3065083.

[37] L. Cai, R. E. White, Reduction of model order based on proper orthogonal decomposition for lithium-ion battery simulations, Journal of The Electrochemical Society 156 (3) (2009) A154. doi:10.1149/1.3049347.

[38] S. v. Erhard, P. J. Osswald, P. Keil, E. Höffer, M. Haug, A. Noel, J. Wilhelm, B. Rieger, K. Schmidt, S. Kosch, F. M. Kindermann, F. Spingler, H. Kloust, T. Thoennessen, A. Rheinfeld, A. Jossen, Simulation and measurement of the current density distribution in lithium-ion batteries by a multi-tab cell approach, Journal of The Electrochemical Society 164 (1) (2017) A6324–A6333. doi:10.1149/2.0551701jes.

[39] K. Smith, C.-Y. Wang, Solid-state diffusion limitations on pulse operation of a lithium ion cell for hybrid electric vehicles, Journal of Power Sources 161 (1) (2006) 628–639. doi:10.1016/j.jpowsour.2006.03.050.

[40] Y. Ji, Y. Zhang, C.-Y. Wang, Li-ion cell operation at low temperatures, Journal of The Electrochemical Society 160 (4) (2013) A636–A649. doi:10.1149/2.047304jes.

[41] J. Smekens, J. Paulsen, W. Yang, N. Omar, J. Deconinck, A. Hubin, J. van Mierlo, A modified multiphysics model for lithium-ion batteries with a LixNi1/3Mn1/3Co1/3O2 electrode, Electrochimica Acta 174 (2015) 615–624. doi:10.1016/j.electacta.2015.06.015.

[42] A. Rheinfeld, J. Sturm, A. Noel, J. Wilhelm, A. Kriston, A. Pfrang, A. Jossen, Quasi-isothermal external short circuit tests applied to lithium-ion cells: Part II. modeling and simulation, Journal of The Electrochemical Society 166 (2) (2019) A151–A177. doi:10.1149/2.0071902jes.

[43] P. R. Nileshwar, A. McGordon, T. R. Ashwin, Greenwood, Parametric optimization study of a lithium-ion cell, Energy Procedia 138 (2017) 829–834. doi:10.1016/j.egypro.2017.10.088.

[44] S. G. Stewart, V. Srinivasan, J. Newman, Modeling the performance of lithium-ion batteries and capacitors during hybrid-electric-vehicle operation, Journal of The Electrochemical Society 155 (9) (2008) A664. doi:10.1149/1.2953524.

[45] W. Fang, O. J. Kwon, C.-Y. Wang, Electrochemical-thermal modeling of automotive Li-ion batteries and experimental validation using a three-electrode cell, International Journal of Energy Research 34 (2) (2010) 107–115. doi:10.1002/er.1652.

[46] H. Lee, M. Yanilmaz, O. Toprakci, K. Fu, X. Zhang, A review of recent developments in membrane separators for

rechargeable lithium-ion batteries, Energy Environ. Sci. 7 (12) (2014) 3857–3886. doi:10.1039/C4EE01432D.

[47] T. R. Tanim, C. d. Rahn, C.-Y. Wang, A temperature dependent, single particle, lithium ion cell model including electrolyte diffusion, Journal of Dynamic Systems, Measurement, and Control 137 (1) (2015) 011005. doi:10.1115/1.4028154.

[48] A. Awarke, S. Pischinger, J. Ogrzewalla, Pseudo 3D modeling and analysis of the SEI growth distribution in large format li-ion polymer pouch cells, Journal of The Electrochemical Society 160 (1) (2013) A172–A181. doi:10.1149/2.022302jes.

[49] C. Capiglia, Y. Saito, H. Kageyama, P. Mustarelli, T. Iwamoto, T. Tabuchi, H. Tukamoto, 7Li and 19F diffusion coefficients and thermal properties of non-aqueous electrolyte solutions for rechargeable lithium batteries, Journal of Power Sources 81-82 (1999) 859–862. doi:10.1016/S0378-7753(98)00237-7.

[50] A. Ehrl, J. Landesfeind, W. A. Wall, H. A. Gasteiger, Determination of transport parameters in liquid binary lithium ion battery electrolytes, Journal of The Electrochemical Society 164 (4) (2017) A826–A836. doi:10.1149/2.1131704jes.

[51] A. Nyman, M. Behm, G. Lindbergh, Electrochemical characterisation and modelling of the mass transport phenomena in LiPF6–EC–EMC electrolyte, Electrochimica Acta 53 (22) (2008) 6356–6365. doi:10.1016/j.electacta.2008.04.023.

[52] L. O. Valoen, J. N. Reimers, Transport properties of LiPF6-based Li-ion battery electrolytes, Journal of The Electrochemical Society 152 (5) (2005) A882. doi:10.1149/1.1872737.

[53] Y.-H. Chen, C.-W. Wang, X. Zhang, A. M. Sastry, Porous cathode optimization for lithium cells: Ionic and electronic conductivity, capacity, and selection of materials, Journal of Power Sources 195 (9) (2010) 2851–2862. doi:10.1016/j.jpowsour.2009.11.044.

[54] M. Park, X. Zhang, M. Chung, G. B. Less, A. M. Sastry, A review of conduction phenomena in li-ion batteries, Journal of Power Sources 195 (24) (2010) 7904–7929. doi:10.1016/j.jpowsour.2010.06.060.

[55] K. Schittkowski, Experimental design tools for ordinary and algebraic differential equations, Industrial & Engineering Chemistry Research 46 (26) (2007) 9137–9147. doi:10.1021/ie0703742.

[56] W. Li, D. Cao, D. Jöst, F. Ringbeck, M. Kuipers, F. Frie, D. U. Sauer, Parameter sensitivity analysis of electrochemical model-based battery management systems for lithium-ion batteries, Applied Energy 269 (2020) 115104. doi:10.1016/j.apenergy.2020.115104.

[57] X.-S. Yang, S. Deb, Cuckoo search via lévy flights, in: World Congress on Nature & Biologically Inspired Computing, 2009, IEEE, Piscataway, N.J., 2009, pp. 210–214. doi:10.1109/NABIC.2009.5393690.

[58] X.-S. Yang, S. Deb, Multiobjective cuckoo search for design optimization, Computers & Operations Research 40 (6) (2013) 1616–1624. doi:10.1016/j.cor.2011.09.026.

[59] X.-S. Yang, S. Deb, Engineering optimisation by cuckoo search, Int. J. Mathematical Modelling and Numerical Optimisation 1 (4) (2010) 330–343. doi:10.1504/IJMMNO.2010.03543.

[60] I. Fister Jr., D. Fister, I. Fister, A comprehensive review of cuckoo search: variants and hybrids, International Journal of Mathematical Modelling and Numerical Optimisation 4 (4) (2013) 387. doi:10.1504/IJMMNO.2013.059205.

[61] M. A. Adnan, M. A. Razzaque, A comparative study of particle swarm optimization and cuckoo search techniques through problem-specific distance function, in: 2013 International Conference of Information and Communication Technology (ICoICT), IEEE, 2013, pp. 88–92. doi:10.1109/icoict.2013.6574619.

[62] W. Li, N. Sengupta, P. Dechent, D. Howey, A. Annaswamy, D. U. Sauer, Online capacity estimation of lithium-ion batteries with deep long short-term memory networks, Journal of Power Sources 482 (2021) 228863. doi:10.1016/j.jpowsour.2020.228863.

[63] W. Li, H. Cui, T. Nemeth, J. Jansen, C. Ünlübayir, Z. Wei, L. Zhang, Z. Wang, J. Ruan, H. Dai, X. Wei, D. U. Sauer, Deep reinforcement learning-based energy management of hybrid battery systems in electric vehicles, Journal of Energy Storage 36 (1) (2021) 102355. doi:10.1016/j.est.2021.102355.

[64] S. Wang, D. Guo, X. Han, L. Lu, K. Sun, W. Li, D. U. Sauer, M. Ouyang, Impact of battery degradation models on energy management of a grid-connected dc microgrid, Energy 207 (2020) 118228. doi:10.1016/j.energy.2020.118228.

[65] W. Li, H. Cui, T. Nemeth, J. Jansen, C. Ünlübayir, Z. Wei, X. Feng, X. Han, M. Ouyang, H. Dai, X. Wei, D. U. Sauer, Cloud-based health-conscious energy management of hybrid battery systems in electric vehicles with deep reinforcement learning, Applied Energy 293 (39) (2021) 116977. doi:10.1016/j.apenergy.2021.116977.

[66] J. Wu, Z. Wei, W. Li, Y. Wang, Y. Li, D. Sauer, Battery thermal- and health-constrained energy management for hybrid electric bus based on soft actor-critic drl algorithm, IEEE Transactions on Industrial Informatics (2020) 1doi:10.1109/TII.2020.3014599.

[67] W. Li, N. Sengupta, P. Dechent, D. Howey, A. Annaswamy, D. U. Sauer, One-shot battery degradation trajectory prediction with deep learning, Journal of Power Sources 506 (1) (2021) 230024. doi:10.1016/j.jpowsour.2021.230024.